Chemical Engineering Journal 435 (2022) 134989

Contents lists available at ScienceDirect

Chemical Engineering Journal

journal homepage: www.elsevier.com/locate/cej

On the concentration models in electrical capacitance tomography for gas-fluidized bed measurements

Anqi Li [a,b], Shuanghe Meng [a,*], Kai Huang [a,c], Wuqiang Yang [d], Mao Ye [a,*]

[a] Dalian National Laboratory for Clean Energy and National Engineering Laboratory for MTO, Dalian Institute of Chemical Physics, Chinese Academy of Sciences, Dalian 116023, Liaoning, China
[b] University of Chinese Academy of Sciences, Beijing 100049, Beijing, China
[c] Joint School of National University of Singapore and Tianjin University, International Campus of Tianjin University, Binhai New City, Fuzhou 350207, China
[d] School of Electrical and Electronic Engineering, The University of Manchester, Manchester M13 9PL, Lancashire, UK

ARTICLE INFO

Keywords:
Gas-fluidized bed
Electrical capacitance tomography
Concentration model
Homogeneous fluidization
Bubble size

ABSTRACT

Electrical capacitance tomography (ECT) has been widely applied in gas-fluidized bed measurements, which however is constrained by the sensor designs, image reconstruction algorithms and concentration models owing to the "soft-field" nature. Among the three factors, the concentration models that map the permittivity to solid concentration distribution are less understood. In this paper we present an experimental investigation on the effects of concentration models for the ECT measurements of gas-fluidized beds containing Geldart's group A particles. The results show that the bubble velocity, bubbling frequency and fluidization regime transition velocity are intrinsic whatever the concentration model employed. However, the time-averaged solid concentrations measured by ECT with the conventional concentration models are usually higher than the corresponding results obtained by the bed expansion experiments in homogeneous fluidization. It has been further found that the concentration models can significantly influence the threshold selection in identifying the bubbles and surrounding emulsion phase in gas-fluidized beds. Thus, a new concentration model given in the formula of a power function ($\boldsymbol{\phi} = \boldsymbol{G}^{\alpha}$) has been proposed, with the optimal exponent α obtained via the least-square fitting of solid concentration in bed expansion during homogeneous fluidization. The model is robust and the sensitivity analysis shows that the variation of time-averaged solid concentration is negligible ($\leq$ 3%) suppose that α changes by $\pm$ 20%.

1. Introduction

Gas-fluidized bed measurements are of extensive significance in understanding the complex hydrodynamics of gas-solids two-phase flows and guiding the engineering scale-up of reactors and associate facilities [1,2]. Now a variety of measurement techniques, classified into intrusive and non-intrusive, have been frequently-used for this purpose, which include the intrusive techniques [3–5] like optical probe, capacitance probe, and pressure measurement, the non-intrusive techniques [6–9] such as digital image analysis (DIA), particle image velocimetry (PIV), X-ray tomography, and magnetic resonance imaging (MRI). Nonetheless, these techniques more or less have shortcomings and/or limitations. The intrusive probes are easy to operate but can only obtain local information of fluidized beds and cannot visualize flow distribution. The non-intrusive techniques such as DIA, PIV and MRI are hard to be used in harsh industrial conditions due to high-cost and complex signal processing although they may offer entire flow regime information [1,2,10]. Electrical capacitance tomography (ECT), owing to the advantages like fast-imaging, non-invasiveness, non-radiation, strong-robustness and low-cost [11], is a versatile and well-recognized technique sparking numerous interests in measuring the gas-solids distribution and hydrodynamic parameters in gas-fluidized beds [12–15]. However, as a "soft-field" technology, ECT shows the relatively low-spatial resolution, which restricts its further industrial applications and meantime stimulates great efforts in promoting the overall performance of ECT [16–20]. Most, if not all, of the ECT studies so far have focused on either the hardware systems or data analysis methods [11,21]. The hardware systems include the ECT sensors and data acquisition equipment, which are essential in acquiring stable and reliable capacitance signals. The data analysis involves the derivation of

* Corresponding authors at: Dalian Institute of Chemical Physics, Chinese Academy of Sciences, Dalian 116023, Liaoning, China.
E-mail addresses: lianqi@dicp.ac.cn (A. Li), mengshh@dicp.ac.cn (S. Meng), maoye@dicp.ac.cn (M. Ye).

https://doi.org/10.1016/j.cej.2022.134989
Received 13 October 2021; Received in revised form 22 December 2021; Accepted 28 January 2022
Available online 2 February 2022

the cross-sectional permittivity distribution using image reconstruction algorithms, and further transformation of the permittivity distribution to the solid concentration distribution (or the solid volume fraction distribution, or the gas-solids distribution) utilizing the so-called concentration models, as plotted in Fig. 1. Key hydrodynamic parameters in gas-fluidized beds, such as solid concentration (time-averaged, and transient) and bubble size, are subsequently analyzed based on the solid concentration distribution.

Therefore, the hardware systems, image reconstruction algorithms, and concentration models constitute the three major concerns in ECT when applying for gas-fluidized bed measurements. For decades, the design of reliable ECT sensors for gas-fluidized bed measurements has received considerable attention. For instance, Wang and Yang [22] studied the effect of the scale-up of sensors and indicated that the sensitivity of the center decreases as the ECT sensor size increases, resulting in the low-quality images in industrial-scale fluidized beds. Huang et al. [16] evaluated the effect of electrode length of ECT sensor in gas-fluidized bed measurements and found that the electrode length should be as short as possible considering the signal-to-noise ratio (SNR) constraint. Recently, Shen et al. [23] also drew similar conclusions and stated that the shorter electrode can minimize the axial-average effect. In terms of ECT image reconstruction, a lot of algorithms have been developed to solve the ill-posed inverse problems. Conventional algorithms include the linear back-propagation (LBP) algorithm [24], Tikhonov regularization algorithm [10,25], Landweber iteration algorithm [26] and so on. These algorithms can be classified into single-step and iterative algorithms [21]. Recently, Chandrasekera et al. [17] developed a total variation iterative soft thresholding (TV-IST) algorithm and found that it is not sensitive to the solid concentration thresholds when extracting bubble diameter information from ECT images.

Nevertheless, the prior studies on ECT for gas-fluidized bed measurements predominantly concentrate on the sensor designs and image reconstruction algorithms. The concentration models, despite the significance in improving the accuracy of ECT measurements [10,12,27–30] being wide-recognized, have been less investigated. McKeen & Pugsley [28] experimentally evaluated three typical concentration models, i.e, series model, parallel model and Maxwell model, against a solid packed bed with an empty tube merging in the middle of the bed, and found that the parallel model can better predict the averge of cross-sectional voidage and recover the equivalent empty tube diameter. In a study on the fluidized bed drying of pharmaceutical granule, Chaplin et al. [30] compared four concentration models (i.e. series model, parallel model, Maxwell model and Böttcher model) for ECT measurements of a fluidized bed with high moisture content, and reported that the Böttcher model gave the best results of the radial profile of solid concentration with reference to the X-ray measurement results. But later on, Wang and Yang [29] found that these concentration models could lead to different ECT measurement resluts for a fluidized bed dryer suppose both the moisture content and flow regimes change. In a simulation study of bubbling fluidized bed, Banaei et al. [27] showed that the inverted-Maxwell model can offer the better ECT results for bubbles with small sizes. Guo et al. [10] reported that the parallel model can give the minimum error (about 5%) in terms of the solid concentration based on the statistics over 78 two-dimensional (2D) gas-solids distributions produced by computational fluid dynamics (CFD) simulations with two-fluid model (TFM). This suggests that the concentration model is critical in obtaining solid concentration, though further experimental verification is required as at this point, there is no guarantee either CFD or concentration model produces reasonable results since both has tunable parameters.

In view of the few yet scattered experimental investigations about the effects of concentration models on ECT in gas-fluidized bed measurements, the primary objective of the present work is to comprehensively study the role of concentration models in practical measurements. For this purpose, the concentration models are experimentally evaluated by measuring pivotal hydrodynamic parameters in gas-fluidized beds. Specifically, the well-defined homogenous bed expansion experiments as well as the hollow glass sphere calibration experiments are carried out to evaluate the concentration models using the transient solid concentration, and time-averaged solid concentration, and bubble size as three direct indicators. Furthermore, an improved and generalized strategy to establish an effective concentration model in ECT for gas-fluidized beds measurements is proposed.

2. Concentration models

As mentioned above, the concentration models are essentially applied to map the permittivity distribution to the solid concentration distribution. Normally, the concentration models are derived based on the principle of mixed permittivity [31]. For gas-solids two-phase flow systems, there are various factors like the permittivity of materials, the phase concentration, the particles shape, the excitation frequency, the system temperature and so on, affecting the mixed permittivity [32]. However, under certain excitation frequency and specified measurement systems, the mixed permittivity can be simply considered as a function of the permittivity and concentration of interest components [18]. In the following, the derivations of concentration models are principally discussed.

2.1. Parallel concentration model

To derive the parallel permittivity model, the two phases between the measuring electrode pairs are assumed to be connected parallelly [28,31]. Thus, for a pixel in ECT, we can obtain

$$\varepsilon^m = \varphi\varepsilon^h + (1-\varphi)\varepsilon^l \tag{1}$$

where ε^m is the permittivity of the mixture, ε^h is the higher-permittivity (i.e., the packed bed permittivity, not the particles permittivity [31]), ε^l is the lower-permittivity (i.e., the fluidization gas permittivity), φ is the solid concentration within a single-pixel. Normalizing Eq. (1) gives

$$\varphi = \frac{\varepsilon^m - \varepsilon^l}{\varepsilon^h - \varepsilon^l} = g \tag{2}$$

with g being the normalized permittivity. By rewriting Eq. (2) to a vector equation, namely parallel concentration model, we can derive

$$\boldsymbol{\phi} = \boldsymbol{G} \tag{3}$$

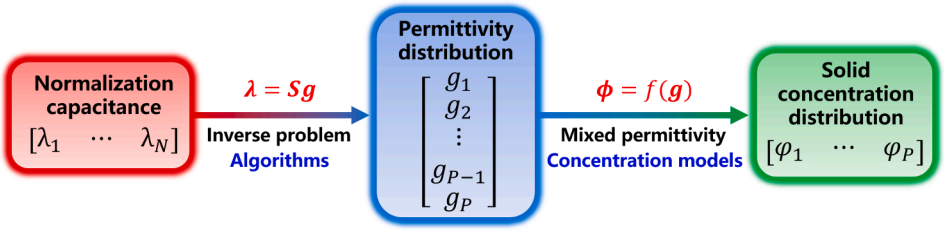

Fig. 1. Schematic diagram of ECT data analysis for gas-fluidized bed measurements.

where $\boldsymbol{\phi} = \begin{bmatrix} \boldsymbol{\varphi}_1 \\ \vdots \\ \boldsymbol{\varphi}_F \end{bmatrix} = \begin{bmatrix} \varphi_{11} & \cdots & \varphi_{1P} \\ \vdots & \ddots & \vdots \\ \varphi_{F1} & \cdots & \varphi_{FP} \end{bmatrix}$ is the normalized solid concentration spatiotemporal distribution vector, $\boldsymbol{G} = \begin{bmatrix} \boldsymbol{g}_1 \\ \vdots \\ \boldsymbol{g}_F \end{bmatrix} = \begin{bmatrix} g_{11} & \cdots & g_{1P} \\ \vdots & \ddots & \vdots \\ g_{F1} & \cdots & g_{FP} \end{bmatrix}$ is the normalized permittivity spatiotemporal distribution vector, F is the total number of sampling frames (in this paper is 5000), P is the number of pixels in a ECT image (in this paper is 3228).

2.2. Maxwell concentration model

The Maxwell permittivity model follows that permittivity of a sphere of higher-permittivity in the lower-permittivity background can be described by Laplace equation [28,31]. In this case, the permittivity of mixture can be written as

$$\varepsilon^m = \varepsilon^l \frac{2\varepsilon^l + \varepsilon^h + 2\varphi(\varepsilon^h - \varepsilon^l)}{2\varepsilon^l + \varepsilon^h - \varphi(\varepsilon^h - \varepsilon^l)} \tag{4}$$

Inverting and normalizing Eq. (4) gives

$$\varphi = \frac{2 + \frac{\varepsilon^h}{\varepsilon^l}}{3 + \frac{\varepsilon^m - \varepsilon^l}{\varepsilon^h - \varepsilon^l} \times \left(\frac{\varepsilon^h}{\varepsilon^l} - 1\right)} \times \frac{\varepsilon^m - \varepsilon^l}{\varepsilon^h - \varepsilon^l} = \frac{(Kr+2)g}{3 + (Kr-1)g} \tag{5}$$

where $Kr = \frac{\varepsilon^h}{\varepsilon^l}$ is the high-low permittivity ratio, and $g = \frac{\varepsilon^m - \varepsilon^l}{\varepsilon^h - \varepsilon^l}$. Rewriting Eq. (5) to a vector equation

$$\boldsymbol{\phi} = \frac{(Kr+2)\boldsymbol{G}}{3 + \boldsymbol{G}(Kr-1)} \tag{6}$$

where the $\boldsymbol{G}$ in Eq. (6) will be treated according to an element-wise division operation.

As can be seen, using the parallel model ($\boldsymbol{\phi} = \boldsymbol{G}$) implies that the permittivity distribution is linearly equivalent to the solid concentration distribution. In contrast, the Maxwell model ($\boldsymbol{\phi} = \frac{(Kr+2)\boldsymbol{G}}{3+\boldsymbol{G}(Kr-1)}$) suggests that the relationship between the two should be nonlinear. And we note that Eq. (3) and Eq. (6) have the same $\boldsymbol{G}$ and Kr, under certain conditions, is a constant, therefore, when we obtain the $\boldsymbol{G}$ under the parallel model (for parallel model, $\boldsymbol{G}$ is equal to $\boldsymbol{\phi}$), the $\boldsymbol{\phi}$ under the Maxwell model can be obtained directly through Eq. (6), i.e., $\boldsymbol{\phi}_{Maxwell} = \frac{(Kr+2)\boldsymbol{\phi}_{parallel}}{3+(Kr-1)\boldsymbol{\phi}_{parallel}}$.

In addition, more concentration models are also derived and summarized in Table 1. Note that the inverted-Maxwell model is obtained by rewriting the Kr of Maxwell model into $1/Kr$, which is designed to adapt the measurements of lower-permittivity objects in higher-permittivity background following Godlieb [31]. Fig. 2 displays the schematic of function formula for different concentration models. As can be seen in Fig. 2, for a given normalized permittivity, the corresponding normalized solid concentration predicted by, in the order of series, Maxwell-Garnett, Maxwell, Böttcher, power-law, parallel, and inverted-Maxwell model, shows an apparent decrease. In the high permittivity region, the Böttcher model almost coincides with the power-law model with $\alpha = 0.5$.

Table 1
Mixed permittivity models and concentration models.

Models	Mixed permittivity models [18]	Concentration models
parallel	$\varepsilon^m = \varphi\varepsilon^h + (1-\varphi)\varepsilon^l$	$\boldsymbol{\phi} = \boldsymbol{G}$
series	$\frac{1}{\varepsilon^m} = \frac{\varphi}{\varepsilon^h} + \frac{(1-\varphi)}{\varepsilon^l}$	$\boldsymbol{\phi} = \frac{Kr\boldsymbol{G}}{1+\boldsymbol{G}(Kr-1)}$
Maxwell	$\varepsilon^m = \varepsilon^l \frac{2\varepsilon^l + \varepsilon^h + 2\varphi(\varepsilon^h - \varepsilon^l)}{2\varepsilon^l + \varepsilon^h - \varphi(\varepsilon^h - \varepsilon^l)}$	$\boldsymbol{\phi} = \frac{(Kr+2)\boldsymbol{G}}{3+\boldsymbol{G}(Kr-1)}$
inverted-Maxwell	$\varepsilon^m = \varepsilon^h \frac{2\varepsilon^h + \varepsilon^l + 2\varphi(\varepsilon^l - \varepsilon^h)}{2\varepsilon^h + \varepsilon^l - \varphi(\varepsilon^l - \varepsilon^h)}$	$\boldsymbol{\phi} = \frac{(2Kr+1)\boldsymbol{G}}{3Kr+\boldsymbol{G}(1-Kr)}$
Maxwell-Garnett	$\varepsilon^m = \varepsilon^l + 2\varphi\varepsilon^l \frac{\varepsilon^h - \varepsilon^l}{\varepsilon^l + \varepsilon^h - \varphi(\varepsilon^h - \varepsilon^l)}$	$\boldsymbol{\phi} = \frac{(Kr+1)\boldsymbol{G}}{2+\boldsymbol{G}(Kr-1)}$
Böttcher	$\frac{\varepsilon^m - \varepsilon^l}{3\varepsilon^m} = \frac{\varphi(\varepsilon^h - \varepsilon^l)}{\varepsilon^h + 2\varepsilon^m}$	$\boldsymbol{\phi} = \frac{Kr\boldsymbol{G}}{3+3\boldsymbol{G}(Kr-1)} + \frac{2}{3}\boldsymbol{G}$
power-law	$(\varepsilon^m)^\alpha = \varphi(\varepsilon^h)^\alpha + (1-\varphi)(\varepsilon^l)^\alpha$	$\boldsymbol{\phi} = \frac{[\boldsymbol{G}(Kr-1)+1]^\alpha - 1}{Kr^\alpha - 1}$

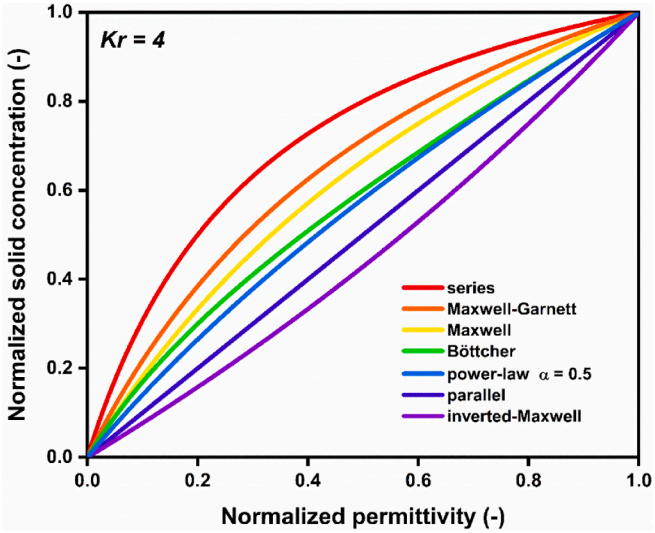

Fig. 2. Mapping normalized permittivity to normalized solid concentration by different concentration models.

3. Experimental

3.1. Experimental setup

To experimentally evaluate the effect of concentration models on the transient and time-averaged solid concentration, and bubble size in gas-fluidized beds by ECT, two sets of experiments were carried out in this study. First of all, the homogeneous fluidization of Geldart's group A particles, in which the gas and solids can be treated as uniformly distributed [33], was considered to assess the performance of different concentration models in obtaining the time-averaged solid concentration. And note that this is homogeneous fluidization so a small fluctuation is also accepted. In this set of experiments, a cold flow fluidized bed reactor made of borosilicate glass column (the glass column permittivity ε^f is 4) was used, which has an inner diameter of 60 mm, height of 1 m, and wall-thickness of 2.5 mm, as shown in Fig. 3a. In the homogeneous bed expansion experiments, the static bed depth of 10 cm was set to weaken the non-uniform distributions of gas and solids and the centerline of the ECT sensor is 5 cm above the gas-distributor. The dried air (the air permittivity ε^l is 1 and air dryness fraction is 99.9%) was uniformly distributed to the bed via a porous gas-distributor made of the expanded polystyrene foam. Air flow rate was monitored by a mass flow controller (Brooks SLA5800, USA). The bed materials used in this set of experiments include three Geldart's group A particles (see supplementary material Figure S1), i.e., two FCC catalysts (FCC I and FCC II) and a Al_2O_3 particles, with the physical properties (including particles density ρ_p, Sauter mean diameter d_p, sphericity δ, particle permittivity ε^p, packed bed solid concentration φ^0, and minimum fluidization velocity U_{mf}) summarized in Table 2. Here the ε^p was measured by the high frequency LCR digital bridge (TH2826, CN) with 180 KHz. And note that the two FCC particles have quite different permittivity. This may be due to that FCC I particles are the fresh catalyst without coke deposition while the FCC II particles are spent catalyst with certain coke deposition.

Then a secondary set of experiments were conducted to assess the performance of concentration models in gas-fluidized bed measure-

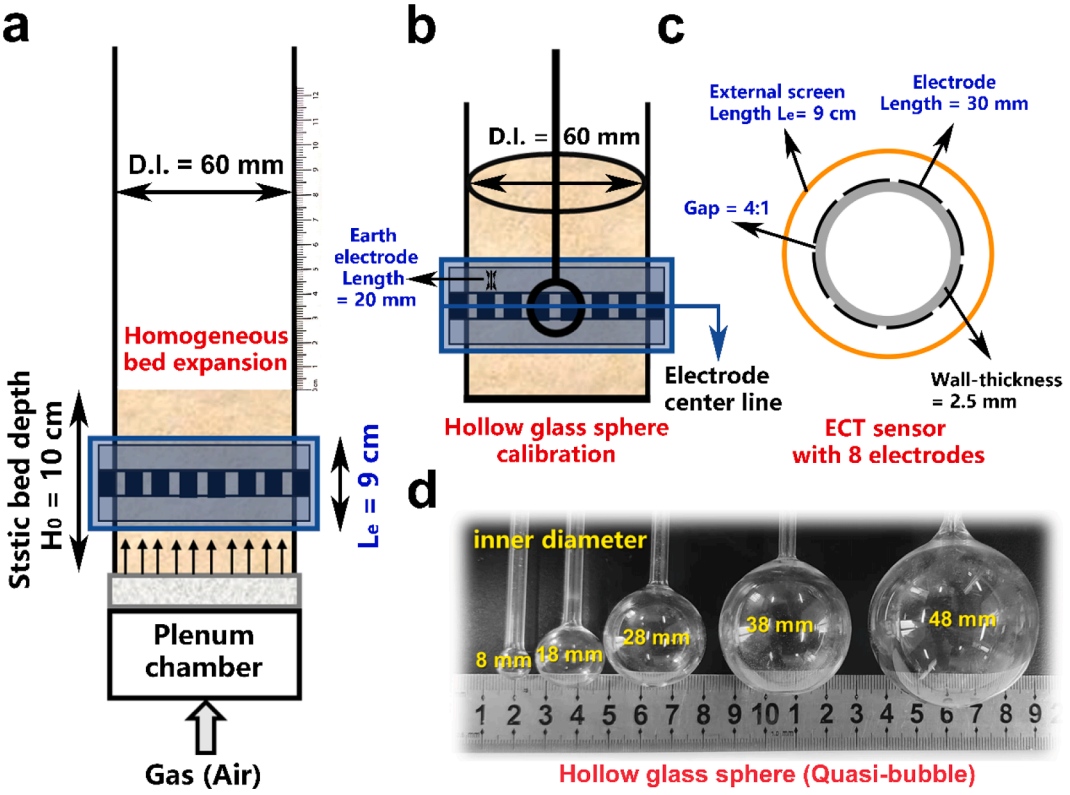

Fig. 3. Schematic diagram of (a) the gas-fluidized bed used in the homogenous bed expansion and bubbling fluidization experiments, (b) the packed bed with hollow glass sphere, (c) the ECT sensor with 8 electrodes, and (d) the hollow glass sphere (called quasi-bubble).

Table 2
Physical properties of bed materials in the assessing measurements.

Particles	Density	Sauter mean diameter	Sphericity	Particle permittivity	Packed solid concentration	Minimum fluidization velocity
	[a] $\rho_p[kg/m^3]$	[b] $d_p[\mu m]$	[c] δ[-]	[d] ε^p[-]	[e] φ^0[-]	[f] $U_{mf}[cm/s]$
FCC I	1400	44.88	0.93	2.96	0.60	0.24
FCC II	1400	83.74	0.92	6.09	0.58	0.47
Al_2O_3	3940	79.16	0.53	8.71	0.43	1.24

[a] The particles density ρ_p was measured by water displacement technique.
[b] The Sauter diameter d_p was calculated by $d_p = \frac{1}{\sum x_i/d_i}$.
[c] The sphericity δ was estimated by SEM images that are added in supplementary material (see supplementary material Figure S2).
[d] The particles permittivity ε^p was measured by the high frequency LCR digital bridge (TH2826, CN) with 180 KHz.
[e] The packed solid concentration φ^0 was calculated from $\varphi^0 = \frac{m}{S \times H_0 \times \rho_p}$, where S is the cross-sectional area of the gas-fluidized bed, and H_0 is the static bed height.
[f] The particle minimum fluidization velocity U_{mf} determined by the ECT curve [34].

ments in presence of non-uniform gas-solids structures such as bubbles. In doing so, hollow glass spheres (quasi-bubbles) with varying diameters (see Fig. 3d) were placed in a stationary picked bed with bed height of 30 cm to simulate gas bubbles in gas-fluidized beds (as shown in Fig. 3b). Five quasi-bubbles with inner diameters of 8, 18, 28, 38 and 48 mm were used. All the hollow glass spheres have wall-thickness of 1 mm (the wall permittivity of hollow glass sphere ε^b is also 4), connecting to a minor glass tube of outer diameter of 5 mm and wall-thickness of 1.5 mm. In the experiments the quasi-bubbles were placed in the center of the sensing region if not specified.

3.2. ECT measurement configuration

In all ECT experiments, the single-plane ECT sensor with 8 electrodes was used. Each electrode has length of 30 mm, the electrode gap ratio is 4:1, the earth electrode used here is 20 mm wide, and the distance between the earth electrode and electrodes is set to 5 mm to minimize the electrostatic interference. The external screen length is 90 mm and the gap between the screen and electrodes is 8 mm.

In ECT image reconstruction, the projected Landweber iteration algorithm was used following Yang & Peng [21] and Guo et al. [10,35]. The formula of the projected Landweber iteration algorithm can be written as

$$\boldsymbol{g}_{k+1} = L[\boldsymbol{g}_k - \theta_k \boldsymbol{S}^T(\boldsymbol{S}\boldsymbol{g}_k - \boldsymbol{\lambda})] \tag{7}$$

where $\boldsymbol{g}$ is the normalized permittivity vector, $\boldsymbol{\lambda} = \frac{\boldsymbol{C}^m - \boldsymbol{C}^l}{\boldsymbol{C}^h - \boldsymbol{C}^l}$ is the normalized capacitance vector (where the $\boldsymbol{C}^m$ is the measured capacitance vector for a random distribution, $\boldsymbol{C}^l$ and $\boldsymbol{C}^h$ are the capacitance vector measured in an empty and packed bed), $\boldsymbol{S}$ is the normalized sensitivity matrix, $\boldsymbol{S}^T$ is the transposed matrix of $\boldsymbol{S}$, θ_k is the optimal step length and k is the index of iteration number. The total of iteration number was set to 200 [10,16]. L is used to constrain $\boldsymbol{g}$ to ensure $\boldsymbol{g} \in [0,1]$. Details of this algorithm can refer to Huang et al. [16] and Guo et al. [34]. Note that $\boldsymbol{\lambda}$

is the measured normalized capacitance by the commercial ECT software, and λ is either 0 or 1 corresponding to respectively the calibration case of empty bed or packed bed. The calibration principles used in this work to map the capacitance to permittivity are essentially the same for both the linear and nonlinear concentration models.

4. Results and discussions

4.1. Transient solid concentration

The transient solid concentration of the gas-fluidized bed was measured by ECT with different concentration models. Fig. 4 shows the results (transient solid concentration fluctuations within 1 s) with Al_2O_3 particles as bed materials, in which seven concentration models (i.e., the series, Maxwell-Garnett, Maxwell, Böttcher, power-law with $\alpha = 0.5$, parallel, and inverted-Maxwell model) were used to map the permittivity distribution to corresponding solid concentration distribution. As can be seen, pronounced difference could be identified for the results obtained by different concentration models. Specifically, the series model produced the highest solid concentration, which is followed by the Maxwell-Garnett, Maxwell, Böttcher, power-law, parallel, and inverted-Maxwell model in order. This is consistent with the results shown in Fig. 2. Meantime, the transient solid concentration obtained by the series model has the smallest fluctuation, and the magnitude of solid concentration fluctuations increases with the order of the Maxwell-Garnett, Maxwell, Böttcher, power-law, parallel, and inverted-Maxwell model. Note that the transient solid concentration fluctuations reflect the passing of flow structures such as gas bubbles in the fluidized beds, it suggests that the series model is relatively insensitive to the flow structures and tiny bubbles, for instance, might be readily missed. Likely the inverted-Maxwell model is the most sensitive to the delicate change of flow structures, and can better reflect the bubble behaviors. Yet, if the ECT algorithms used are prone to artifacts, the inverted-Maxwell model will also magnify these, so an extra care is needed when using such as Tikhonov regularization algorithm [10]. Moreover, a close check with the transient solid concentration fluctuations in Fig. 4 shows that the results obtained by different concentration models are qualitatively consistent, indicating that the bubble velocity, bubbling frequency and fluidization transition velocity (i.e., U_{mf}, U_{mb}) are intrinsic regardless of the concentration models used. This is also confirmed by the time–frequency analysis of transient solid concentration (see supplementary material Figure S3 and S4).

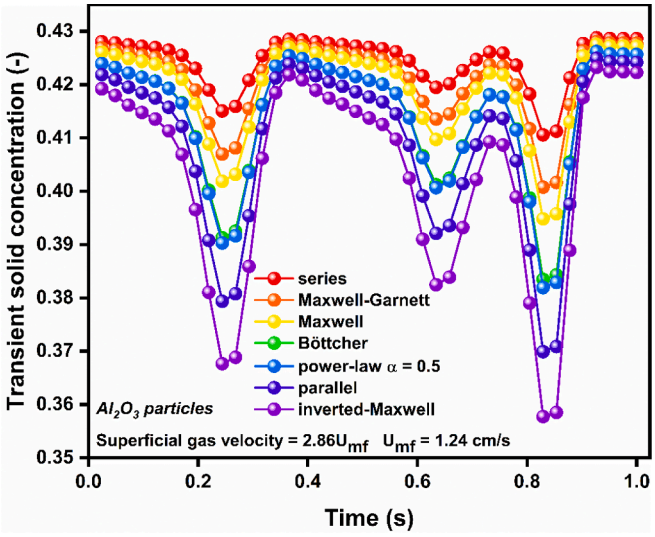

Fig. 4. Transient solid concentration obtained by different concentration models. The fluidized particles are Al_2O_3, the static bed depth is 60 cm and the centerline of the ECT sensor is 50 cm above the gas-distributor. The superficial gas velocity is $2.86U_{mf}^{Al_2O_3}$ with $U_{mf}^{Al_2O_3} = 1.24cm/s$.

4.2. Time-averaged solid concentration

The time-averaged solid concentration is an essential industrial parameter in gas-fluidized bed measurements. In ECT, it can be generally defined as [34,36]

$$\overline{\boldsymbol{\phi}} = \varphi^0 \frac{\sum_{f=1}^{F}\sum_{p=1}^{P}\boldsymbol{\phi}}{F \times P} \tag{8}$$

where the packed solid concentration φ^0 is defined in Table 2, the two-level summation notation $\sum_{f=1}^{F}\sum_{p=1}^{P}\boldsymbol{\phi}$ indicates the summation over all elements of the matrix $\boldsymbol{\phi}$. Furthermore, it in the homogeneous fluidization regime can also be obtained by the following formula [37]

$$\overline{\boldsymbol{\phi}} = \frac{m}{S \times H \times \rho_p} \tag{9}$$

where m is the mass of particles in the packed bed, H is the homogeneous bed expansion height, as shown in Fig. 3a, the bed height H was measured by a flexible scale fixed in the fluidized bed wall and was recorded after 10 min of stable operation at a given gas flow velocity.

In this section, the bed expansion experiments of three Geldart's group A particles were carried out to evaluate the performance of these models with regard to the time-averaged solid concentration. As mentioned above, owing to the uniform axial solid concentration distribution in the homogeneous fluidization regime of Geldart's group A particles, we consider the average solid concentration of whole bed equivalently as the time-averaged solid concentration in the local position of ECT sensor. Fig. 5 presents the variation of time-averaged solid concentration for these three particles (i.e., FCC I, FCC II, and Al_2O_3) in the homogeneous fluidization regime based on the homogeneous bed expansion experiments. As can be seen, the time-averaged solid concentration decreases with the increasing superficial gas velocity, indicating the dilution of the gas-solids systems at higher gas velocity, which is consistent with the ECT measurement trends. In Fig. 5c the trends for the Al_2O_3 particles seem to be linearly decreasing, compared to the trends of FCC particles. This may be due to that the Al_2O_3 particles are at located at the boundary between group A and B particles in the Geldart's group fluidization diagram (see supplementary material Figure S1). Hence the interval of the homogeneous fluidization regime of the Al_2O_3 particles is narrow, which will cause the transition from a packed bed to bubbling fluidization is relatively sharp. And a similar phenomenon was also shown in a recent experimental study [34].

However, the time-averaged solid concentrations measured by ECT, regardless of the concentration models used, are higher than that obtained by bed expansion experiments for all three particles. Furthermore, as the superficial gas velocity increases, the ECT measurement results deviate further from that obtained by the homogeneous bed expansion. Among all seven concentration models, the inverted-Maxwell model shows relatively better performance for all three particles. Based on the discussions, we showed that the ECT fails to quantitatively measure the time-averaged solid concentration utilizing the existing concentration models, which has not been well-recognized in the field [28,30].

4.3. Bubble size in gas-fluidized beds

4.3.1. Static experiments with hollow glass spheres

Bubble size plays an important role in designing gas-fluidized bed reactors, and ECT is one of the major visualization methods widely used for measuring bubble size [15,17]. However, owing to the ambiguous boundary between bubbles and emulsion phase in gas-fluidized beds as well as the low-spatial resolutions of ECT [10,17,38], extracting the bubble size from the ECT gas-solids distribution images depends

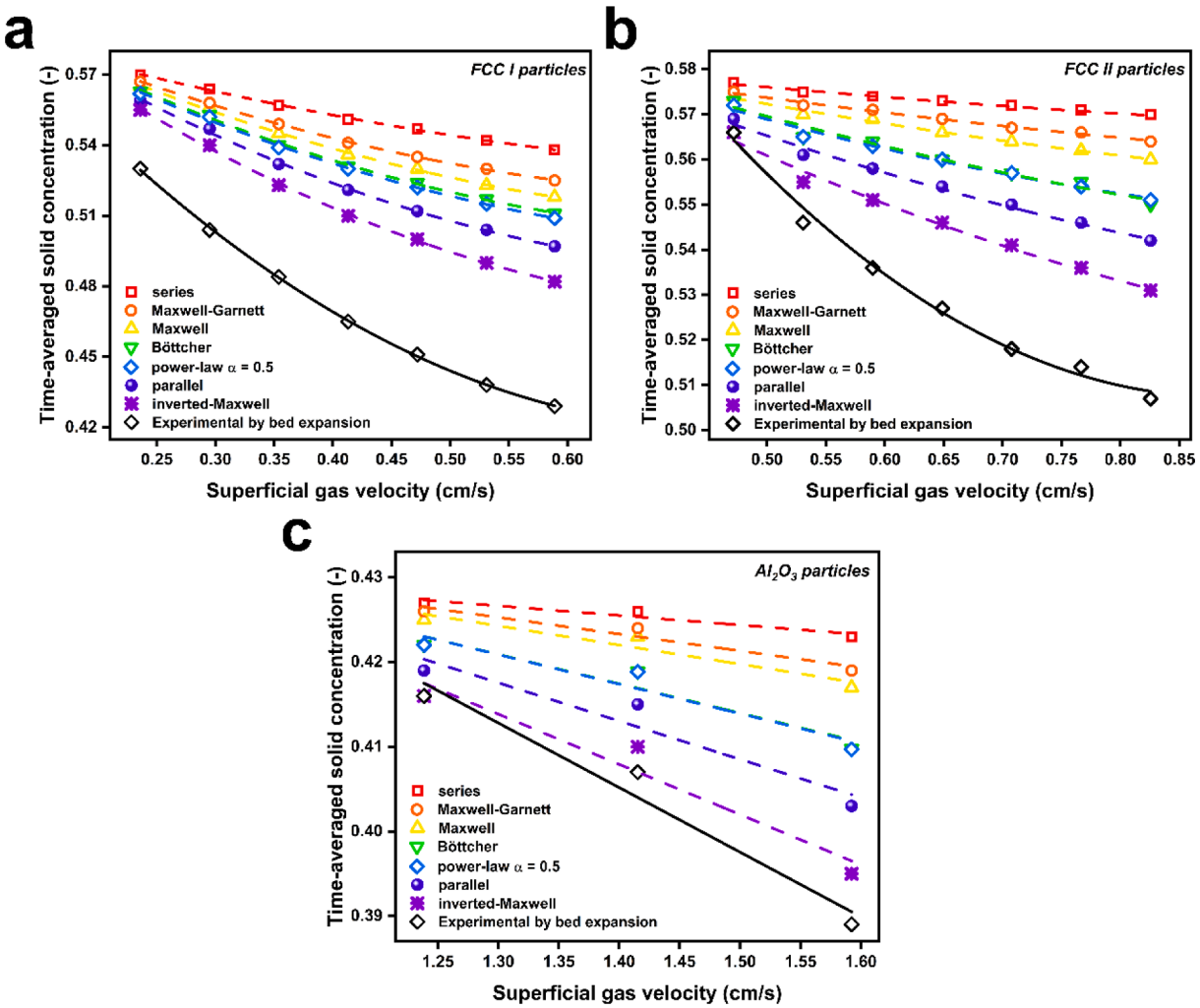

Fig. 5. Comparison of time-averaged solid concentration measured by the ECT with different concentration models and the homogeneous bed expansion experiments. The fluidized particles are (a) FCC I, (b) FCC II, and (c) Al_2O_3, the static bed depth is 10 cm and the centerline of the ECT sensor is 5 cm above the gas-distributor.

essentially on a critical cutoff of solid concentration (or threshold) [39]. Though many methods have been developed to determine the threshold [39–43], the hollow glass sphere calibration is proverbially implemented in most of applications [39,40]. Hence, this method will also be used in this work to evaluate the concentration models in ECT for bubble size measurements. To minimize the interference of wall-thickness of these hollow glass sphere, we selected the material of glass bubbles by matching its permittivity as close as possible to the that of the packed bed so that the wall-thickness of the glass bubbles can be treated as part of the packed beds, following most of the works [39,40]. In fact, the wall-thickness of glass bubbles used in our work was strictly set as 1 mm for all experiments, and we argued that such a thin wall-thickness would possess negligible impacts. In addition, it was previously shown that the effect of wall-thickness of fluidized bed could be insignificant if the relative wall-thickness of a fluidized bed satisfies $\frac{R_o-R_i}{R_o} < 16.67\%$ [44]. In our current work, the relative wall-thickness is about 7.69% (whereR_o = 32.5 mm is the outer semidiameter, R_i=30 mm is the inner semi-diameter), which may have only a minor effect on the ECT image reconstruction.

The solid concentration distribution of the packed beds in presence of a single quasi-bubble was measured by ECT with different concentration models. Quasi-bubbles with five different inner diameters, i.e., 8, 18, 28, 38 and 48 mm, were examined. Fig. 6 displays the results obtained by four typical concentration models, i.e., series, Maxwell, parallel, and inverted-Maxwell model, in a packed bed filled with Al_2O_3 particles. Where the quasi-bubbles were placed in the center of the sensing region. But it should be noted that these operations were conducted manually during the experiments, and minor deviation of the positions of the glass bubbles of about 2 mm were observed, which caused some eccentricity in the results. In this paper, our main purpose is to assess the concentration models, we argued that the effects causing by such minor deviations would be insignificant. As observed, for all concentration models assessed, the small bubble with a diameter of 8 mm cannot be captured, which is line with the Figure 9 of Shen et al. [23]. This may be due to the fact that the volume of quasi-bubble of 8 mm is less than 1% of the entire sensing region [23]. For bubbles larger than 18 mm, the inverted-Maxwell model presents the relatively optimal results. This may be due to that the inverted-Maxwell model better reproduces the bubbles-emulsion phase structure, namely the continuous high permittivity emulsion phases contain the low permittivity bubbles [31]. Furthermore, these models do not change the shape of gas-solids distribution.

Furthermore, these quasi-bubble diameters obtained by changing different concentration models and thresholds were compared. Fig. 7 show the heatmaps of the concentration models and thresholds for recovering the actual quasi-bubble diameters of 18, 28, 38, and 48 mm. Here we define the area value in the heatmaps larger than the actual quasi-bubble diameter as gray, the quasi-bubble diameter can be read by

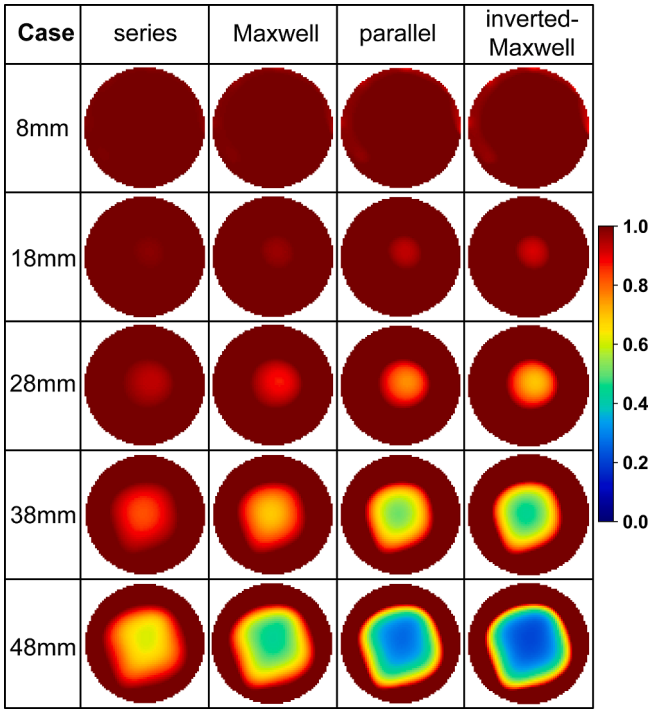

Fig. 6. Solid concentration distributions of the packed beds in presence of single quasi-bubble measured by the ECT with different concentration models. The packed particles are Al_2O_3. The Colorbar represents the normalized solid concentration.

determining a concentration model and a threshold. Overall, it can be clearly seen that the threshold required to obtain the actual diameter of a specified quasi-bubble decrease when the concentration model is chosen in the order of the series, Maxwell, parallel and inverted-Maxwell model. This suggests that the bubble size calculated is highly dependent on the concentration model and threshold. More specifically, taking Fig. 7d as an example, to recover the quasi-bubble diameter of 48 mm as best as possible, we need to choose a normalized threshold (the ratio of the critical cutoff of solid concentration to the packed bed solid concentration φ^0) as high as 0.99 when using the series model, while 0.9 when using the inverted-Maxwell model. Note that the quasi-bubble diameter of 48 mm still cannot be obtained (only 45.2 mm) by using the inverted-Maxwell model with a threshold of 0.99. This can be also possibly attributed to the electrodes design and insensitivity of central zone for ECT [16,22,23]. However, for the quasi-bubble diameter of 18 and 28 mm (< electrode length of 30 mm), when using respectively the Maxwell, parallel, inverted-Maxwell model with a threshold of 0.99, the calculated quasi-bubble diameters are higher than actual.

Further Fig. 8 shows the effect of ratio of actual quasi-bubble diameter to electrode length ($\frac{d^{actual}_{quasibubble}}{L_{electrode}}$) on the relative quasi-bubble diameter ($\frac{d^{calculated}_{quasibubble}}{d^{actual}_{quasibubble}}$) obtained by ECT using different concentration models and thresholds. For a lower threshold of 0.8, as $\frac{d^{actual}_{quasibubble}}{L_{electrode}}$ increases from 0.27 to 1.6, $\frac{d^{calculated}_{quasibubble}}{d^{actual}_{quasibubble}}$ also increases from 0 to 0.6 ~ 0.9 for different models. The increasing tendency shows a *J*-shape for series model and *S*-shape for other models. For a higher threshold of 0.99, $\frac{d^{calculated}_{quasibubble}}{d^{actual}_{quasibubble}}$ increases first and then becomes a constant (about 0.93) after $\frac{d^{actual}_{quasibubble}}{L_{electrode}} > 1$ when using the series model, however, $\frac{d^{calculated}_{quasibubble}}{d^{actual}_{quasibubble}}$ initially increases, subsequently decreases, and then becomes a constant (about 0.94) when using the Maxwell, parallel, and inverted-Maxwell model. Furthermore, it can be seen that the higher threshold of 0.99 can offset the issue of compressed bubble size (i.e., $\frac{d^{calculated}_{quasibubble}}{d^{actual}_{quasibubble}} > 1$) when $0.66 < \frac{d^{actual}_{quasibubble}}{L_{electrode}} < 1.1$. In other cases, $\frac{d^{calculated}_{quasibubble}}{d^{actual}_{quasibubble}}$ becomes less than 1 regardless of the threshold taken. Generally speaking, the accurate acquisitions of bubble sizes require carefully selecting thresholds that depend on both the bubble size and concentration models used. Whilst there is a range of thresholds that will yield a similar result, no single threshold would be applicable across the whole range of bubble sizes. This also indicates that more synergistic work in the future is needed by considering the image reconstruction algorithms, hardware, and concentration models simultaneously to eliminate this issue in ECT measurements.

4.3.2. *Bubbling fluidization experiments*

To gain further insight into the effect of concentration models on the bubble size for the actual particles systems, we studied the bubble behaviors in a bubbling-slugging fluidized bed containing the Al_2O_3 particles using different concentration models (the range of superficial gas velocity is 2.4 ~ 3.6 cm/s). The bubble sizes measured by ECT [15] with four typical concentration models, as function of superficial gas velocities, are shown in Fig. 9 (details of calculation are added in the supplementary material, see Figure S5 ~ S7). These results have been also compared with the predictions by empirical correlations of Mori and Wen [45] and Darton et al. [46]

$$D_b = D_{b\infty} - (D_{b\infty} - D_{b0})\exp(-0.3\frac{h}{D}) \tag{10}$$

$$D_b = 0.54\left(U - U_{mf}\right)^{0.4}(h + 4\sqrt{A_0})^{0.8}g^{-0.2} \tag{11}$$

where $D_{b\infty} = 1.49[D^2(U - U_{mf})]^{0.4}$ and $D_{b0} = 0.376(U - U_{mf})^2$. Here h is the height above the gas-distributor, A_0 the gas-distributor characteristic parameter, and$A_0 = 0$ for porous gas-distributor. For convenience, the operating aspect ratio (the ratio of the bed depth to bed diameter) of fluidized bed was set to 10 (corresponding the actual bed depth is 60 cm) so that a typical deep bed was achieved and a stable single-bubble (a slug) passing through the ECT measurement region (the centerline of the ECT sensor is 50 cm above the gas-distributor) could be detected for certain gas velocities [47]. Here the normalized thresholds of 0.465, 0.8, 0.9, and 0.98 were chosen to calculate the bubble diameters, and we assume that the zone between the two correlations is the precise averaged bubble diameter zone. From the figure we can see that for the normalized threshold of 0.465 (the actual threshold is 0.2) the calculations of bubble diameters are seriously underestimated (< 10 mm) for the four models, however, in some other works [15,48], the bubble size can be well calculated by the threshold of 0.2. We think this may be related to the particle properties, reactor size and operating conditions. Specifically, it might be due to the type of slugging during the experiments. From the Figures 3 and 5 in the paper by Agu et al. [48], we can find that their operational regimes were more like the wall-slugging, however, in our work, the regimes are essentially center-slugging. The position of slugging in the fluidized bed would affect the choice of threshold. When using the series and Maxwell model, the optimal normalized threshold is 0.98 or so, which is much higher than the thresholds of 0.7 ~ 0.9 [36,49]. And if using the parallel, inverted-Maxwell model, the optimal is about 0.9. All models with an optimal threshold are able to reflect the averaged bubble size and trends. However, compared to detecting the quasi-bubble with diameters of 38 mm and 48 mm, the optimal threshold of 0.9 in the bubbling fluidization experiments is lower than the optimal threshold of 0.99 (see Fig. 8) in the hollow glass sphere calibration experiments, this may be due to that the presence of a certain amount of gas in the emulsion phase so that the bubbles are more easily identified.

In general, the accurate quantification of bubble size in ECT measurements is related to many factors, including but not limited to the

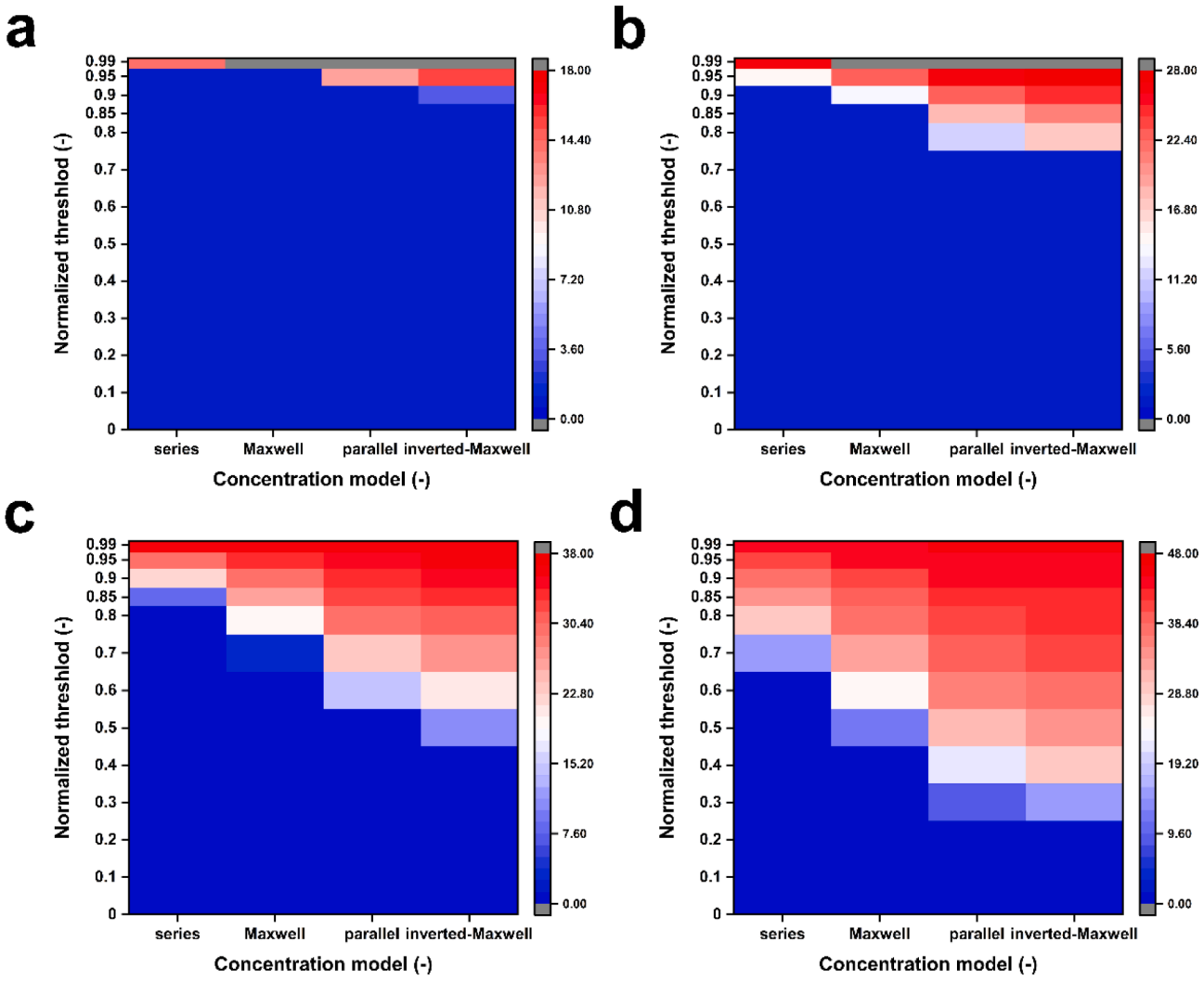

Fig. 7. Effect of concentration models and thresholds on quasi-bubble diameter obtained by ECT. The actual quasi-bubble diameter is (a) 18 mm, (b) 28 mm, (c) 38 mm, (d) 48 mm. The Colorbar represents calculated quasi-bubble diameter.

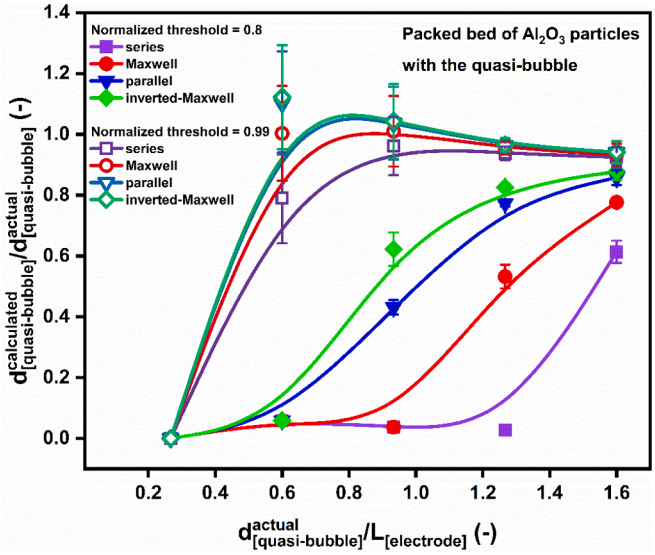

Fig. 8. Effect of ratio of actual quasi-bubble diameter to electrode length on calculated quasi-bubble diameter obtained by ECT.

reconstruction algorithm, concentration model, and threshold of solid concentration. As shown in this work, the role of concentration model in bubble size determination cannot be omitted. However, using some of the listed mixing models, unreasonably high threshold is needed to fit the bubble size with empirical correlations. A high threshold may lead to a narrow adjustable range for the solid concentration during the bubble identification, which is not conducive to the accurate measurements of bubble size and sometimes magnifies artifacts.

4.4. A general strategy of concentration model

From above discussion, it is known that the conventional concentration models have to be improved in order to obtain the accurate results of the solid concentration and bubble size. Here we found that a general concentration model, which is given in the format of a power function, can better represent the relation between the permittivity distribution and gas-solids distribution in gas-fluidized beds,

$$\phi = G^{\alpha} \tag{11}$$

where α is a fitting parameter obtained by the least-square fitting of the solid concentration in the homogeneous fluidization regime (here only for Geldart's group A particles). The schematic representations of the proposed concentration model for $\alpha = 1.5$, 2 and 3 are illustrated respectively in Fig. 10.

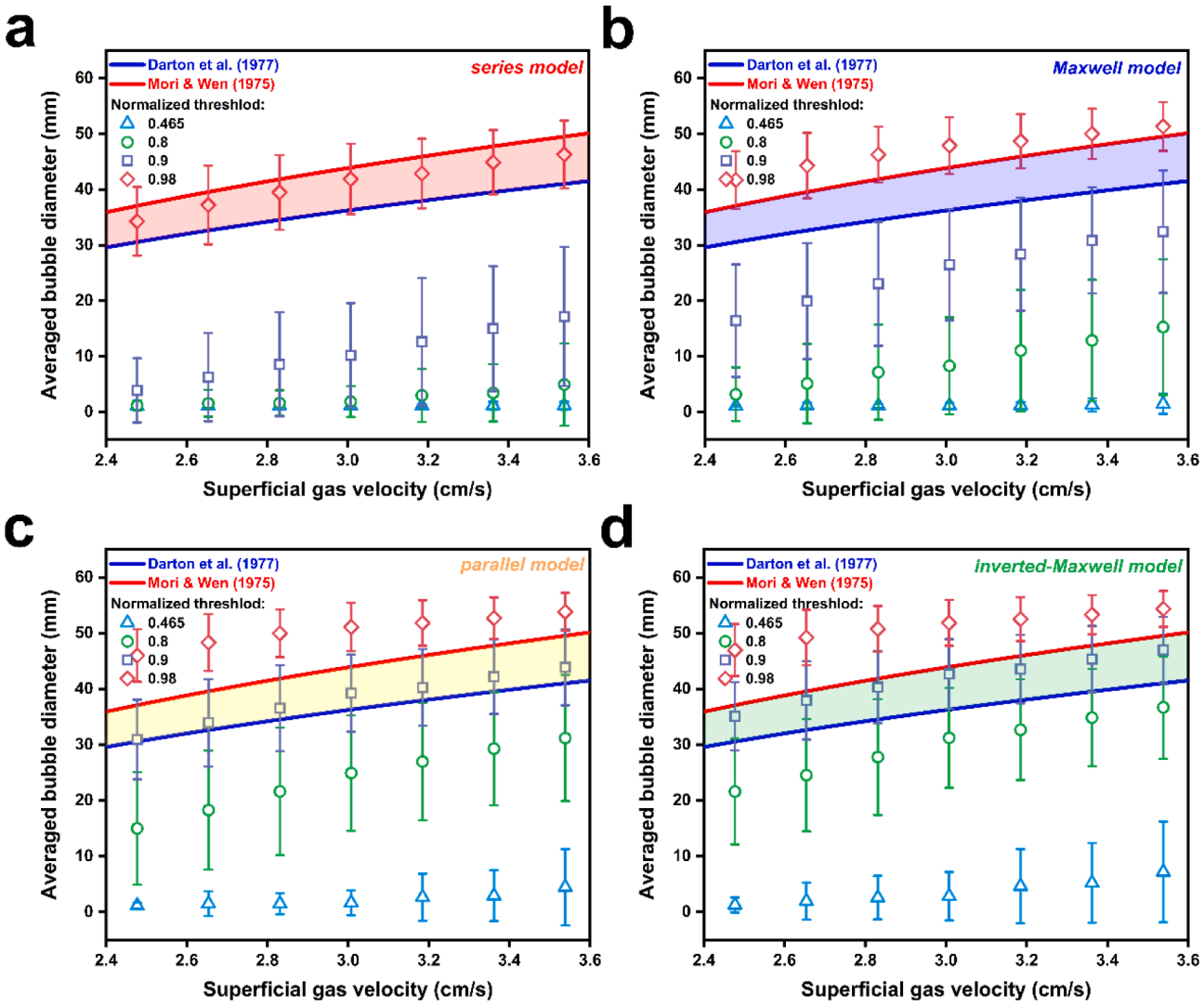

Fig. 9. Averaged bubble diameter calculated by (a) series, (b) Maxwell, (c) parallel, and (d) inverted-Maxwell concentration model with different thresholds. The fluidized particles are Al_2O_3, the static bed depth is 60 cm and the centerline of the ECT sensor is 50 cm above the gas-distributor.

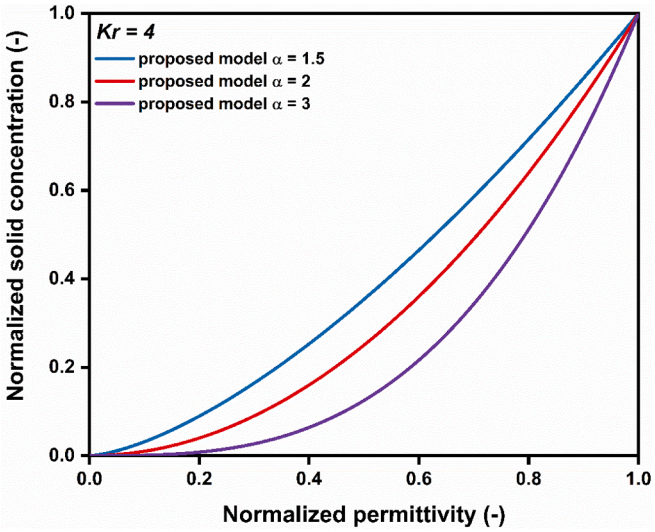

Fig. 10. Mapping normalized permittivity to normalized solid concentration by the proposed concentration model ($\phi = G^{\alpha}$) with different exponents (α = 1.5, 2, and 3).

4.4.1. *Proposed model for time-averaged solid concentration*

To validate the feasibility of the proposed concentration model, Fig. 11 compares the time-averaged solid concentration measured by the homogeneous bed expansion experiments and that measured by ECT with the proposed model for three kinds of particles mentioned above. In the Section 4.2, we could find that the time-averaged solid concentration measured by ECT using the conventional concentration models deviate essentially from that directly measured with bed expansion experiments, and the deviations become larger as the time-averaged solid concentration decreases. Here the optimal fitting parameter α is 2 for FCC type of particles while 1.5 for Al_2O_3 particles. As can be seen, the time-averaged solid concentration measured by ECT using the proposed model with an optimal α is in accordance with the results obtained by the homogeneous bed expansion experiments for all gas velocities, with the errors being within 3%. To investigate the sensitivity of α, we artificially changed α by ± 20%. From Fig. 11 we found that the results of time-averaged solid concentration become higher if α was reduced by 20% and lower if α was increased by 20%. However, the overall errors still fall within ± 3%, indicating the robustness of the proposed model, i.e., the variation of time-averaged solid concentration are negligible (≤ 3%) suppose that α changes by ± 20%.

Fig. 12 further shows how the model responds to the minor changes in the optimal fitting parameter α. The sensitivity of α is different for

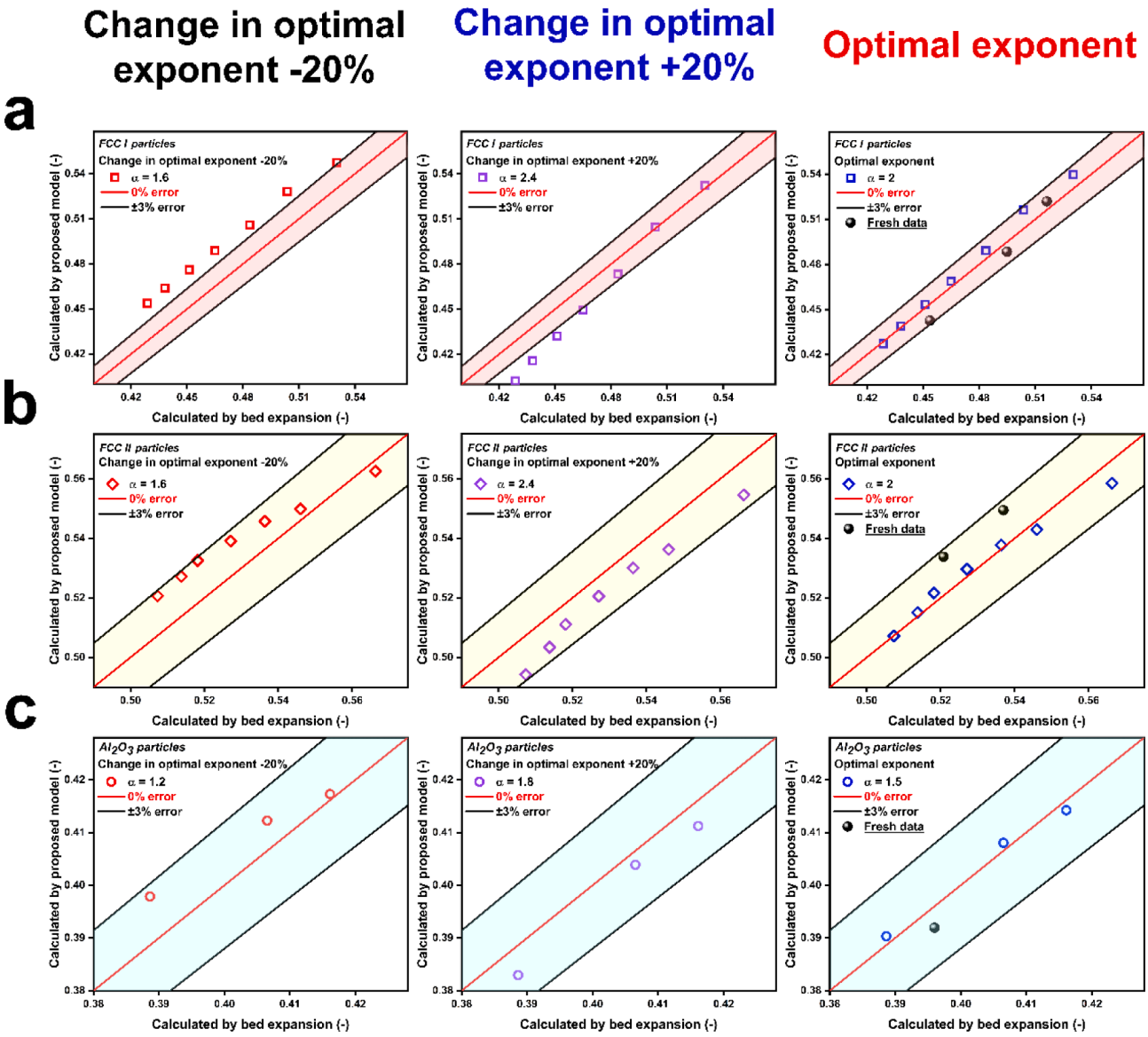

Fig. 11. Comparison of time-averaged solid concentration measured by the ECT with the proposed concentration model ($\phi = G^{\alpha}$) and the homogeneous bed expansion experiments. The fluidized particles are (a) FCC I, (b) FCC II, and (c) Al_2O_3, the static bed depth is 10 cm.

different particles systems. Considering the ± 3% error span, the changeable span of optimal parameter α is about −30%~35% for the FCC II and Al_2O_3 particles, about −10%~20% for FCC I particles. We also conducted some additional experiments, and the data from these additional experiments were used as the test data set (see the black dots). It is found that these additional data can fit the model prediction very well for different particle systems, suggesting the model is genetic and robust.

4.4.2. *Proposed model for bubble size*

We also tried to reconstruct the solid concentration distribution with ECT using the series, Maxwell, parallel, inverted-Maxwell, and proposed model for the situation that a quasi-bubble was immersed in the gas-fluidized bed, and obtained the quasi-bubble diameter. Fig. 13 shows the average relative error of diameter of three quasi-bubbles with inner diameters of 28, 38, and 48 mm respectively. Here, a normalized threshold of 0.9 was chosen to identify the boundaries of these quasi-bubbles. As can be seen, for the quasi-bubble with an inner diameter of 28 mm, the series model results in an average relative error of up to 97%, while the inverted-Maxwell model about 20%. It is also noteworthy that for the quasi-bubble with larger diameters (i.e., 38 and 48 mm), the difference between the results obtained by the parallel model and that by inverted-Maxwell model reduced, with the errors being within 20%. The proposed concentration model, meantime, manifests the minimum relative errors, about 17%. In addition, as shown in Fig. 14, the single-bubbling (or slugging) regimes for three particles systems (FCC I, FCC II, and Al_2O_3) in the gas-fluidized bed were also visualized by ECT with the proposed concentration model, compared with other models. Here we specify that the lower solid concentration is, the darker red color of the marker is. And these single-bubbles are profiled with the contours of 0.7, 0.8, and 0.9 respectively. As mentioned above, the solid concentration distributions obtained by using the conventional series model are high, so that the contours of 0.7 cannot be presented in these cases. The presentation of these bubbles is enhanced with the order of the series, Maxwell, parallel, and inverted-Maxwell model. However, in terms of bubble size, due to the higher threshold, there is still a lot of room for improvement. Further we reused the proposed model to reconstruct these single-bubbling regimes, from the figure we can found that the proposed model outperforms other in the identification of gas-solids distribution.

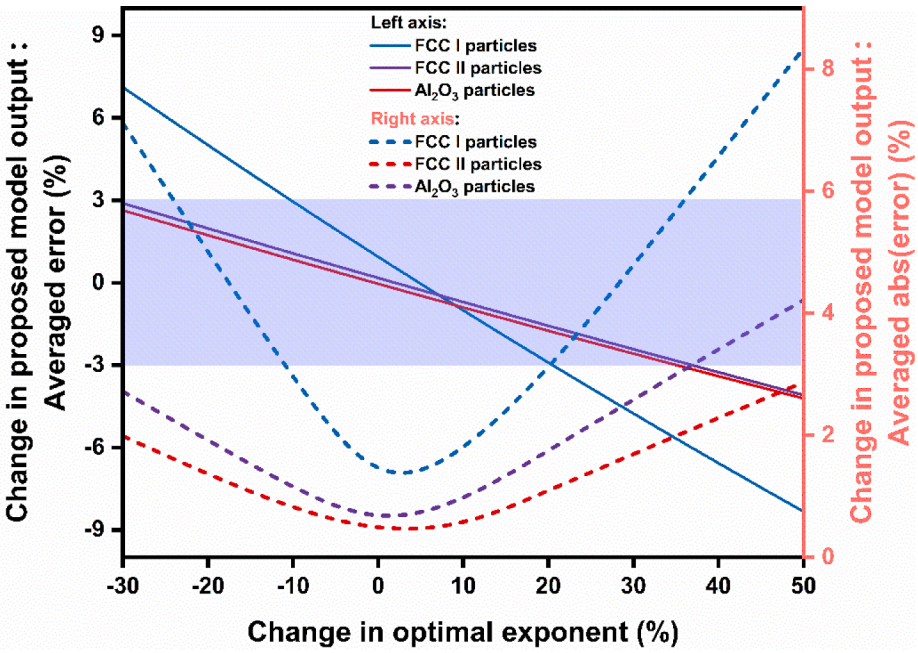

Fig. 12. Response of the proposed concentration model ($\phi = G^{\alpha}$) for changes in the model exponent.

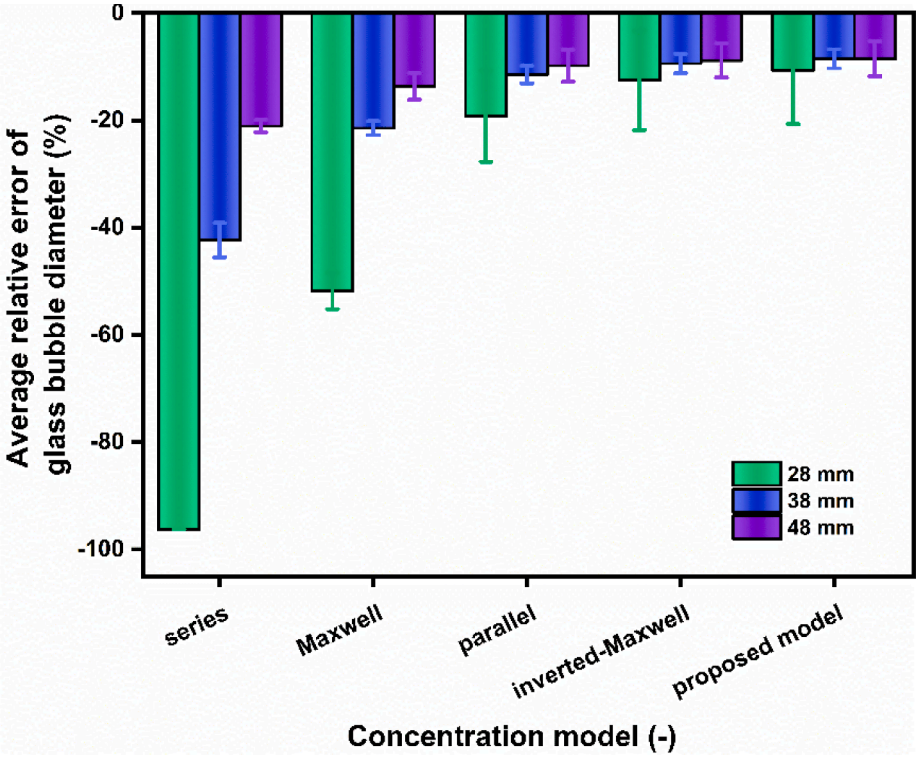

Fig. 13. Effect of the proposed concentration model ($\phi = G^{\alpha}$) on the average relative error of quasi-bubble diameter. The threshold is 0.9.

5. Conclusions

Concentration models play an essential role in mapping the permittivity to solid concentration distribution. In this paper, the effects of concentration models on the key hydrodynamic parameters (time-averaged and transient solid concentration, and bubble size) in gas-fluidized bed measurements are investigated through a series of experiments (i.e., the homogenous bed expansion experiments of Geldart's group A particles, the hollow glass sphere calibration experiments, and the bubbling fluidization experiments). In addition, a power law model has been proposed. Based on this work, the following conclusions are drawn:

(a) The time–frequency analysis of transient solid concentration fluctuations shows that the hydrodynamic parameters of such as bubble velocity, bubbling frequency and fluidization transition velocity are not affected by the choice of concentration model.

(b) The homogeneous bed expansion experiments of Geldart's group A particles show that the time-averaged solid concentration measured

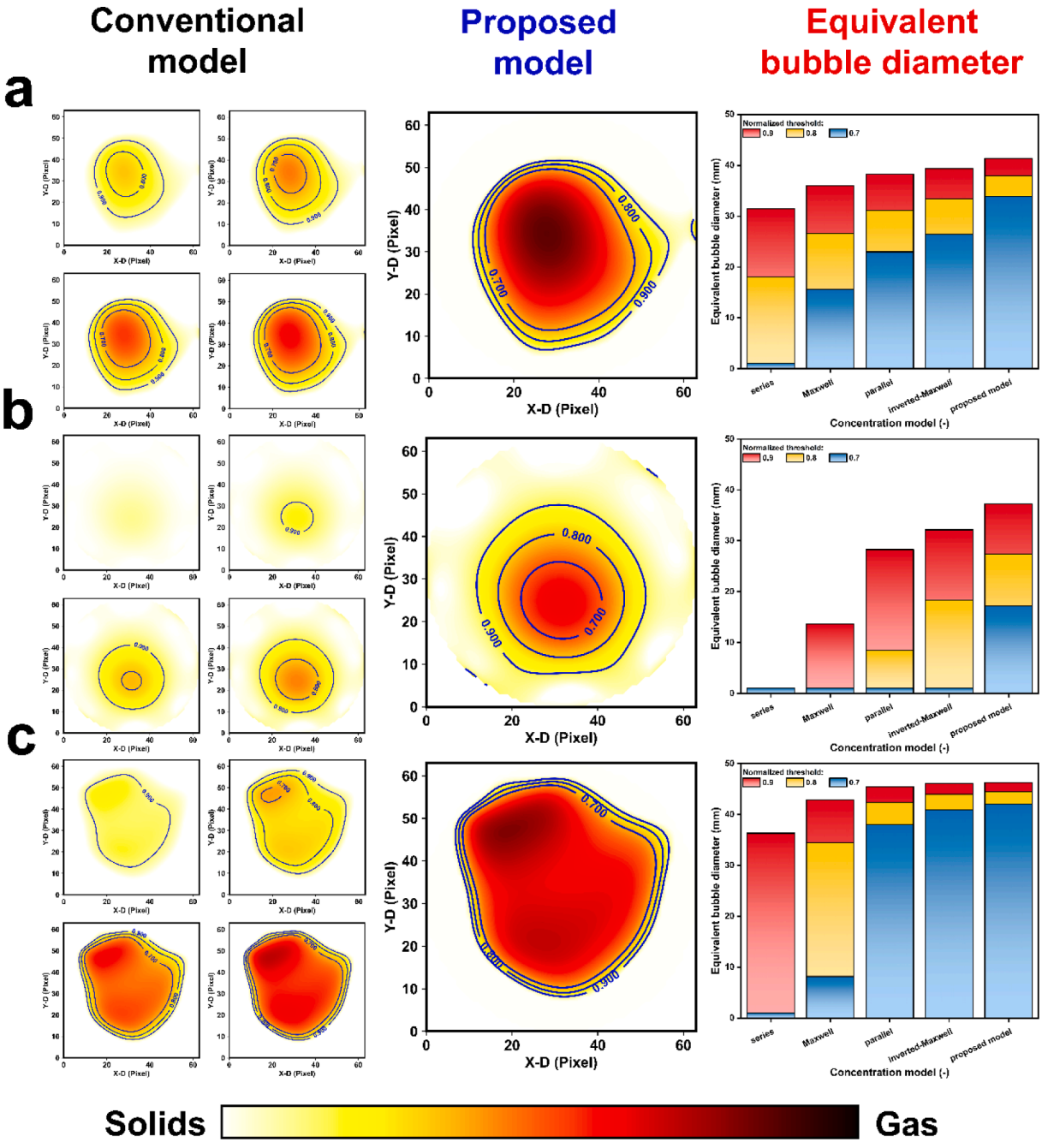

Fig. 14. Contour diagram of the actual single-bubbling regimes (the darker red color, the higher gas). The fluidized particles are (a) FCC I, (b) FCC II, and (c) Al_2O_3. The superficial gas velocities are (a) $3.75U_{mf}^{FCCI}$, $U_{mf}^{FCCI} = 0.24cm/s$, (b) $3.13U_{mf}^{FCCII}$, $U_{mf}^{FCCII} = 0.47cm/s$, (c) $2.86U_{mf}^{Al_2O_3}$, $U_{mf}^{Al_2O_3} = 1.24cm/s$. For all cases, the static bed depth is 60 cm and the centerline of the ECT sensor is 50 cm above the gas-distributor. (For interpretation of the references to color in this figure legend, the reader is referred to the web version of this article.)

by ECT with the conventional concentration models (i.e., the series, Maxwell-Garnett, Maxwell, Böttcher, power-law with $\alpha = 0.5$, parallel, and inverted-Maxwell model) are usually higher than the results obtained by the homogeneous bed expansion, which has not been well-recognized in the field.

(c) The hollow glass sphere calibration experiments show that the accurate acquisitions of bubble sizes require carefully selecting thresholds that depend on both the bubble size and concentration models used. Whilst there is a range of thresholds that will yield a similar result, no threshold would be applicable across the whole range of bubble sizes.

(d) As shown in this work, the role of concentration model in bubble size determination cannot be omitted. When using some of the listed mixing models, unreasonably high threshold is needed to fit the bubble size with empirical correlations. However, A high threshold may lead to a narrow adjustable range for the solid concentration during the bubble identification, which is not conducive to the accurate measurements of bubble size and sometimes magnifies artifacts.

(e) A general strategy for concentration model given in the formula of a power function has been proposed. It is found that, if the optimal fitting exponent α is obtained by the least-square fitting of solid concentration in homogeneous fluidization regime of Geldart's group A particles, the proposed model can better represent the relation between the permittivity distribution and solid concentration distribution in gas-fluidized beds. The sensitivity analysis of model shows that the model

output seems unaffected (error $\leq$ 3%) by changes in optimal parameter α within $\pm$ 20%.

Although the proposed model has shown good performance for Geldart's group A particles, extending this model to more general applications still need to be further explored with regards to the electrodes design, image reconstruction algorithms, particles and fluid properties, reactor size, and among many others. In future works, it will be interesting to synergistically check the sensitivity of proposed model to these factors within a wider range in ECT measurements of gas-fluidized beds.

Declaration of Competing Interest

The authors declare that they have no known competing financial interests or personal relationships that could have appeared to influence the work reported in this paper.

Acknowledgements

The authors are grateful to the National Natural Science Foundation of China (Grant No. 91834302).

Appendix A. Supplementary data

Supplementary data to this article can be found online at https://doi.org/10.1016/j.cej.2022.134989.

References

[1] J.R. van Ommen, R.F. Mudde, Measuring the gas-solids distribution in fluidized beds: A review, Int. J. Chem. React. Eng. 6 (2008), https://doi.org/10.2202/1542-6580.1796.
[2] J. Sun, Y. Yan, Non-intrusive measurement and hydrodynamics characterization of gas-solid fluidized beds: A review, Meas. Sci. Technol. 27 (11) (2016) 112001, https://doi.org/10.1088/0957-0233/27/11/112001.
[3] C.X. Wang, J. Zhu, S. Barghi, C.Y. Li, Axial and radial development of solids holdup in a high flux/density gas-solids circulating fluidized bed, Chem. Eng. Sci. 108 (2014) 233–243, https://doi.org/10.1016/j.ces.2013.12.042.
[4] C.M.H. Brereton, J.R. Grace, Microstructural aspects of the behaviour of circulating fluidized beds, Chem. Eng. Sci. 48 (14) (1993) 2565–2572, https://doi.org/10.1016/0009-2509(93)80267-T.
[5] J.R. van Ommen, S. Sasic, J. van der Schaaf, S. Gheorghiu, F. Johnsson, M.-O. Coppens, Time-series analysis of pressure fluctuations in gas-solid fluidized beds: A review, Int. J. Multiphas. Flow. 37 (5) (2011) 403–428, https://doi.org/10.1016/j.ijmultiphaseflow.2010.12.007.
[6] A.V. Patil, E.A.J.F. Peters, V.S. Sutkar, N.G. Deen, J.A.M. Kuipers, A study of heat transfer in fluidized beds using an integrated DIA/PIV/IR technique, Chem. Eng. J. 259 (2015) 90–106, https://doi.org/10.1016/j.cej.2014.07.107.
[7] F. Hernandez-Jimenez, S. Sanchez-Delgado, A. Gomez-Garcia, A. Acosta-Iborra, Comparison between two-fluid model simulations and particle image analysis & velocimetry (PIV) results for a two-dimensional gas-solid fluidized bed, Chem. Eng. Sci. 66 (2011) 3753–3772, https://doi.org/10.1016/j.ces.2011.04.026.
[8] V. Verma, J.T. Padding, N.G. Deen, J.A.M.H. Kuipers, F. Barthel, M. Bieberle, M. Wagner, U. Hampel, Bubble dynamics in a 3D gas-solid fluidized bed using ultrafast electron beam X-ray tomography and two-fluid model, AIChE J. 60 (5) (2014) 1632–1644, https://doi.org/10.1002/aic.14393.
[9] A. Penn, T. Tsuji, D.O. Brunner, C.M. Boyce, K.P. Pruessmann, C.R. Muller, Real-time probing of granular dynamics with magnetic resonance, Sci. adv. 3 (2017), e1701879, https://doi.org/10.1126/sciadv.1701879.
[10] Q. Guo, S. Meng, D. Wang, Y. Zhao, M. Ye, W. Yang, Z. Liu, Investigation of gas-solid bubbling fluidized beds using ECT with a modified Tikhonov regularization technique, AIChE J. 64 (1) (2018) 29–41, https://doi.org/10.1002/aic.15879.
[11] W.Q. Yang, Design of electrical capacitance tomography sensors, Meas. Sci. Technol. 21 (2010), 042001.
[12] H.G. Wang, W.Q. Yang, Application of electrical capacitance tomography in circulating fluidised beds: A review, Appl. Therm. Eng. 176 (2020), 115311, https://doi.org/10.1016/j.ces.2020.116236.
[13] R. Ge, J. Ye, H. Wang, W. Yang, Measurement of particle concentration in a wurster fluidized bed by electrical capacitance tomography sensors, AIChE J. 60 (12) (2014) 4051–4064, https://doi.org/10.1002/aic.14595.
[14] C.E. Agu, L.A. Tokheim, M. Eikeland, B.M.E. Moldestad, Determination of onset of bubbling and slugging in a fluidized bed using a dual-plane electrical capacitance tomography system, Chem. Eng. J. 328 (2017) 997–1008, https://doi.org/10.1016/j.cej.2017.07.098.
[15] C.E. Agu, C. Pfeifer, M. Eikeland, L.-A. Tokheim, B.M.E. Moldestad, Models for predicting average bubble diameter and volumetric bubble flux in deep fluidized beds, Ind. Eng. Chem. Res. 57 (7) (2018) 2658–2669, https://doi.org/10.1021/acs.iecr.7b04370.
[16] K. Huang, S. Meng, Q. Guo, W. Yang, T. Zhang, M. Ye, Z. Liu, Effect of electrode length of an electrical capacitance tomography sensor on gas-solid fluidized bed measurements, Ind. Eng. Chem. Res. 58 (47) (2019) 21827–21841, https://doi.org/10.1021/acs.iecr.9b03988.
[17] T.C. Chandrasekera, Y. Li, D. Moody, M.A. Schnellmann, J.S. Dennis, D.J. Holland, Measurement of bubble sizes in fluidised beds using electrical capacitance tomography, Chem. Eng. Sci. 126 (2015) 679–687, https://doi.org/10.1016/j.ces.2015.01.011.
[18] B. Hadi, F. Berruti, C. Briens, New calibration methods for accurate electrical capacitance tomography measurements in particulate-fluid systems, Ind. Eng. Chem. Res. 48 (1) (2009) 274–280, https://doi.org/10.1021/ie800292d.
[19] H. Wu, B. Buschle, Y.J. Yang, C. Tan, F. Dong, J.B. Jia, M. Lucquiaud, Liquid distribution and hold-up measurement in counter current flow packed column by electrical capacitance tomography, Chem. Eng. J. 353 (2018) 519–532, https://doi.org/10.1016/j.cej.2018.07.016.
[20] S. Wang, J. Li, M. Kong, C. Xu, S. Wang, Electrostatic effect on AC-based ECT and its elimination, IEEE Sens. J. 17 (24) (2017) 8081–8090.
[21] W.Q. Yang, L.H. Peng, Image reconstruction algorithms for electrical capacitance tomography, Meas. Sci. Technol. 14 (2003) R1–R13.
[22] H. Wang, W. Yang, Scale-up of an electrical capacitance tomography sensor for imaging pharmaceutical fluidized beds and validation by computational fluid dynamics, Meas. Sci. Technol. 22 (10) (2011) 104015, https://doi.org/10.1088/0957-0233/22/10/104015.
[23] J. Shen, S. Meng, M. Ye, W. Yang, Z. Liu, 3D image reconstruction using an ECT sensor with a single layer of electrodes, Meas. Sci. Technol. 31 (8) (2020) 085106, https://doi.org/10.1088/1361-6501/ab82c0.
[24] C.G. Xie, S.M. Huang, M.S. Beck, B.S. Hoyle, R. Thorn, C. Lenn, D. Snowden, Electrical capacitance tomography for flow imaging - system model for development of image-reconstruction algorithms and design of primary sensors, IEE Proc. G (Circuits Dev. Syst.) 139 (1) (1992) 89, https://doi.org/10.1049/ip-g-2.1992.0015.
[25] L. Jing, S. Liu, L.i. Zhihong, S. Meng, An image reconstruction algorithm based on the extended Tikhonov regularization method for electrical capacitance tomography, Measurement 42 (3) (2009) 368–376, https://doi.org/10.1016/j.measurement.2008.07.003.
[26] W.Q. Yang, D.M. Spink, T.A. York, H. McCann, An image-reconstruction algorithm based on Landweber's iteration method for electricalcapacitance tomography, Meas. Sci. Technol. 10 (1999) 1065–1069, https://doi.org/10.1088/0957-0233.
[27] M. Banaei, M. van Sint Annaland, J.A.M. Kuipers, N.G. Deen, On the accuracy of Landweber and Tikhonov reconstruction techniques in gas-solid fluidized bed applications, AIChE J. 61 (12) (2015) 4102–4113, https://doi.org/10.1002/aic.14976.
[28] T.R. McKeen, T.S. Pugsley, The influence of permittivity models on phantom images obtained from electrical capacitance tomography, Meas. Sci. Technol. 13 (12) (2002) 1822–1830, https://doi.org/10.1088/0957-0233/13/12/304.
[29] H.G. Wang, W.Q. Yang, Measurement of fluidised bed dryer by different frequency and different normalisation methods with electrical capacitance tomography, Powder Technol. 199 (1) (2010) 60–69, https://doi.org/10.1016/j.powtec.2009.04.019.
[30] G. Chaplin, T. Pugsley, L.V.D. Lee, A. Kantzas, C. Winters, The dynamic calibration of an electrical capacitance tomography sensor applied to the fluidized bed drying of pharmaceutical granule, Meas. Sci. Technol. 16 (6) (2005) 1281–1290, https://doi.org/10.1088/0957-0233/16/6/007.
[31] W. Godlieb, High Pressure Fluidization, Technical University of Twente, Enschede, The Netherlands, 2010.
[32] A.H. Sihvola, Electromagnetic Mixing Formulas and Applications, London, U. K, Institution of Electrical Engineers, 1999.
[33] Y. Jin, Overview, in: Y. Jin, J.X. Zhu, Z.W. Wang, Z.Q. Yu (Eds.), Fluidization engineering principles, TsingHua University Press, Beijing, PR, China (in Chinese), 2001.
[34] Q. Guo, S. Meng, Y. Zhao, L. Ma, D. Wang, M. Ye, W. Yang, Z. Liu, Experimental verification of solid-like and fluid-like states in the homogeneous fluidization regime of Geldart A particles, Ind. Eng. Chem. Res. 57 (7) (2018) 2670–2686, https://doi.org/10.1021/acs.iecr.7b0455910.1021/acs.iecr.7b04559.s00110.1021/acs.iecr.7b04559.s002.
[35] Q. Guo, X. Li, B. Hou, G. Mariethoz, M. Ye, W. Yang, Z. Liu, A novel image reconstruction strategy for ECT: Combining two algorithms with a graph cut method, IEEE Trans. Instrum. Meas. 69 (3) (2020) 804–814.
[36] X. Zhu, P. Dong, Z. Zhu, R. Ocone, W. Yang, H. Wang, Effects of pressure on flow regimes transition velocities and bubble properties in a pilot-scale pressurised circulating fluidised bed, Chem. Eng. J. 410 (2021) 128438, https://doi.org/10.1016/j.cej.2021.128438.
[37] J.-P. Couderc, Incipient fluidization and particulate systems, in: J.F. Davidson, R. Clift, D. Harrison (Eds.), Fluidization (2nd edition)1985, p. 10.
[38] Y.G. Yates, D.J. Cheesman, Y.A. Sergeev, Experimental observations of voidage distribution around bubbles in a fluidized bed, Chem. Eng. Sci. 49 (12) (1994) 1885–1895, https://doi.org/10.1016/0009-2509(94)80073-1.
[39] V. Agrawal, Y.H. Shinde, M.T. Shah, R.P. Utikar, V.K. Pareek, J.B. Joshi, Estimation of bubble properties in bubbling fluidized bed using ECVT measurements, Ind. Eng. Chem. Res. 57 (24) (2018) 8319–8333, https://doi.org/10.1021/acs.iecr.8b00349.
[40] R.B. White, Using electrical capacitance tomography to monitor gas voids in a packed bed of solids, Meas. Sci. Technol. 13 (12) (2002) 1842–1847, https://doi.org/10.1088/0957-0233/13/12/306.
[41] B. Du, W. Warsito, L.-S. Fan, Bed nonhomogeneity in turbulent gas-solid fluidization, AIChE J. 49 (5) (2003) 1109–1126, https://doi.org/10.1002/aic.690490506.

[42] H.T. Bi, P.-C. Su, Local phase holdups in gas-solids fluidization and transport, AIChE J. 47 (9) (2001) 2025–2031, https://doi.org/10.1002/aic.690470913.
[43] N. Otsu, A threshold selection method from grey-level histogram, IEEE Trans. Syst. Man Cybern. 9 (1979) 62–66.
[44] S. Liang, J. Ye, H. Wang, M. Wu, W. Yang, Influence of the internal wall thickness of electrical capacitance tomography sensors on image quality, Meas. Sci. Technol. 29 (3) (2018) 035401, https://doi.org/10.1088/1361-6501/aaa0a1.
[45] S. Mori, C.Y. Wen, Estimation of bubble diameter in gaseous fluidized beds, AIChE J. 21 (1) (1975) 109–115, https://doi.org/10.1002/aic.690210114.
[46] R. Darton, R.D. Lanauze, J.F. Davidson, D. Harrison, Bubble growth due to coalescence in fluidized beds, Trans. Inst. Chem. Eng. 55 (1977) 274–280.
[47] J. Baeyens, D. Geldart, An investigation into slugging fluidized beds, Chem. Eng. Sci. 29 (1) (1974) 255–265, https://doi.org/10.1016/0009-2509(74)85051-7.
[48] C.E. Agu, A. Ugwu, C. Pfeifer, M. Eikeland, L.A. Tokheim, B.M.E. Moldestad, Investigation of bubbling behavior in deep fluidized beds at different gas velocities using electrical capacitance tomography, Ind. Eng. Chem. Res. 58 (2019) 2084–2098, https://doi.org/10.1021/acs.iecr.8b05013.
[49] A. Bakshi, C. Altantzis, R.B. Bates, A.F. Ghoniem, Multiphase-flow statistics using 3D detection and tracking algorithm (MS3DATA): methodology and application to large-scale fluidized beds, Chem. Eng. J. 293 (2016) 355–364, https://doi.org/10.1016/j.cej.2016.02.058.